

## Structural study of FeP<sub>2</sub> at high pressure

X. Wu<sup>a\*</sup>, M. Kanzaki<sup>b</sup>, S. Qin<sup>c</sup>, G. Steinle-Neumann<sup>a</sup> and L. Dubrovinsky<sup>a</sup>

<sup>a</sup>*Bayerisches Geoinstitut, University Bayreuth, Bayreuth, Germany;* <sup>b</sup>*Institute for Study of the Earth's Interior, Okayama University, Misasa, Tottori, Japan;* <sup>c</sup>*Department of Geology, Peking University, Beijing, China*

(Received 2 September 2008; final version received 4 November 2008)

The structural stability of marcasite-type FeP<sub>2</sub> at high pressure has been studied by X-ray diffraction, Raman spectroscopy, and theoretical calculations. Experimental results show that no phase transitions happen up to 28 GPa at room temperature. The shortest axis of the marcasite-type FeP<sub>2</sub> cell, the *c*-axis, is the most compressible, due to the softening of edge-shared octahedra along the *c*-axis. The linear pressure coefficients and Grüneisen parameters of four Raman modes are determined. Theoretical calculations further support the experimental results and indicate that FeP<sub>2</sub> is still a semiconductor up to 35 GPa.

**Keywords:** marcasite-type structure; high pressure; theoretical calculations

### 1. Introduction

Among MX<sub>2</sub>-type compounds (M: transition metal; X: S, Se, Te, N, P, As, Sb), the marcasite-type structure (*Pnmm*) is very common [1–11]. In the marcasite structure, cations occupy Wyckoff position 2a (0, 0, 0) and anions are located at Wyckoff position 4g (*x*, *y*, 0). Each cation has a deformed octahedral environment, and octahedra share edges along the *c*-axis. The *c/a* ratio and cation *d*-electron configuration are used to classify marcasites as “anomalous marcasite” and “regular marcasite” [1,2]. The regular marcasite has a small *c/a* ratio of 0.53–0.57 and a *d<sup>n</sup>* configuration with *n* ≤ 4 for cations, whereas the anomalous marcasite has a large *c/a* ratio of 0.73–0.75 and a *d<sup>n</sup>* configuration with *n* ≥ 6 for cations.

Iron phosphide FeP<sub>2</sub> crystallizes in the regular marcasite structure at ambient conditions with *c/a* = 0.55 and a *d<sup>4</sup>* configuration with no unpaired spins in a low-spin configuration, as indicated by its diamagnetic nature [3,4]. FeP<sub>2</sub> is a semiconductor with a small band gap of 0.37 eV [3], which could potentially be used in photoelectrochemical cells and solar chargeable batteries [12,13]. A semiconductor-to-metal crossover is reported in an analogue material FeSb<sub>2</sub> with strong magnetic fluctuation at low temperature [14,15].

At various temperature and (or) pressure conditions, the marcasite-type compounds have a number of different polymorphs. Pyrite and the marcasite phases are observed in FeS<sub>2</sub> [5].

---

\*Corresponding author. Email: xiang.wu@uni-bayreuth.de

Marcasite-type  $\text{NiAs}_2$  transforms into a parammelsbergite-type phase at 853 K [6], and a high-pressure pyrite-type phase of  $\text{NiP}_2$  has been synthesized [7]. At high temperature and pressure,  $\text{CrSb}_2$  transforms into the tetragonal  $\text{CuAl}_2$ -type structure, where each Cr atom is coordinated by eight Sb atoms and two Cr atoms [8,9]. Goodenough [10] has described energy bands of  $\text{MX}_2$  compounds with pyrite, marcasite, and arsenopyrite structures in detail. The various structures lead to diverse physical properties. For example,  $\text{CuSe}_2$  has a higher superconducting critical temperature in the pyrite structure than the marcasite structure [11], and the bulk modulus of the pyrite-type superhard material  $\text{PtN}_2$  is higher than that of the marcasite-type [16].

In contrast to these compounds, there is no information about the behavior of  $\text{FeP}_2$  at high pressure that would explore this potentially rich physical behavior. Here, we combine experimental and computational work to explore structural stability, physical properties, and their underlying causes in  $\text{FeP}_2$  under pressure. We perform *in situ* X-ray diffraction (XRD) and Raman spectroscopy (RS) measurements up to 28 GPa and underpin the data by density functional theory (DFT)-based electronic structure calculations. In the following section, we introduce the methods used in the current study, and then present experimental and computational results and their relation. A discussion of the results in terms of crystallographic and electronic structure follows before conclusions are given.

## 2. Methods

The  $\text{FeP}_2$  sample was synthesized by the standard solid-state reaction. Stoichiometric amounts of Fe (99.99%) and red P (99.99%) were mixed and ground in an agate mortar. The mixture was loaded in a sealed and evacuated silicon tube, which was heated at 900 °C for 48 h. Then it was cooled to room temperature for several hours. The product was examined by XRD, with results showing a single marcasite-structured phase, without any impurity.

The high-pressure device in our work is a four-pin modified Merrill–Basset design diamond anvil cell (DAC) with 450  $\mu\text{m}$  culets. A 250  $\mu\text{m}$ -diameter hole was drilled in the pre-indented 55  $\mu\text{m}$  rhenium gasket. LiF was used as pressure-transmitting medium. A small ruby chip was loaded for pressure calibration [17]. The XRD patterns were recorded by a system consisting of a high-brilliance FRD rotating anode generator (Mo  $K\alpha\lambda$  radiation,  $\lambda = 0.7108 \text{ \AA}$ ) and Bruker APEX charge-coupled device (CCD) area detector. Collecting time of each pattern was 30 min. All collected patterns were integrated using the Fit2D program [18] in order to obtain conventional one-dimensional diffraction spectra.

Micro-Raman spectra were recorded in back-scattering geometry using Dilor X–Y spectrometer with a liquid nitrogen cooled CCD detector, 50 $\times$  objective, and confocal mode. Excitation was performed using the 514.5 nm line of  $\text{Ar}^+$  ion laser. The incident laser power was 35 mW. The acquisition time of each spectrum was 15 min.

The DFT-based computations were performed within the full potential linearized augmented plane wave (FP-LAPW)+local orbitals (lo) method, implemented in the WIEN2K code [19,20]. The exchange-correlation potential was treated by the local spin density approximation (LSDA) [21]. The muffin-tin radii of Fe and P were chosen as 1.9 and 1.7 bohr, and kept constant for all compressions studied. We set the energy threshold between core and valence states at  $-7.0 \text{ Ry}$ . The muffin-tin radius multiplied by  $K_{\text{max}}$  was chosen as 7.0, where  $K_{\text{max}}$  is the plane wave cut-off. In the whole Brillouin zone (BZ), 1000  $k$ -points were specified. In our calculations, all unit-cell parameters were optimized at constant volume. Computations were performed on a dense volume set for both marcasite-structured  $\text{FeP}_2$  and other  $\text{MX}_2$  structure types: Pyrite ( $Pa-3$ ),  $\text{CuAl}_2$  ( $I4/mcm$ ), and  $\alpha\text{-PbO}_2$  ( $Pbcn$ ).

### 3. Results and discussions

#### 3.1. X-ray powder diffraction

XRD data were collected up to 28 GPa at room temperature. Figure 1 shows several selected patterns. All peaks can be indexed as marcasite-type  $\text{FeP}_2$  and  $\text{LiF}$  (pressure-transmitting medium). No phase transition was observed. The unit-cell parameters were refined by a full-profile model refinement (Le Bail method) using the GSAS software [22]. We also tried to refine the atomic coordinates, but the R factor is too big, possibly due to the pressure gradient arising from the solid pressure-transmitting medium and the larger size of the X-ray beam. At ambient conditions, lattice parameters ( $a = 4.980(3) \text{ \AA}$ ,  $b = 5.665(3) \text{ \AA}$ ,  $c = 2.723(1) \text{ \AA}$ , and  $V = 76.86(5) \text{ \AA}^3$ ) are consistent with previous results [4]. Unit-cell parameters of  $\text{FeP}_2$  at various pressures are listed

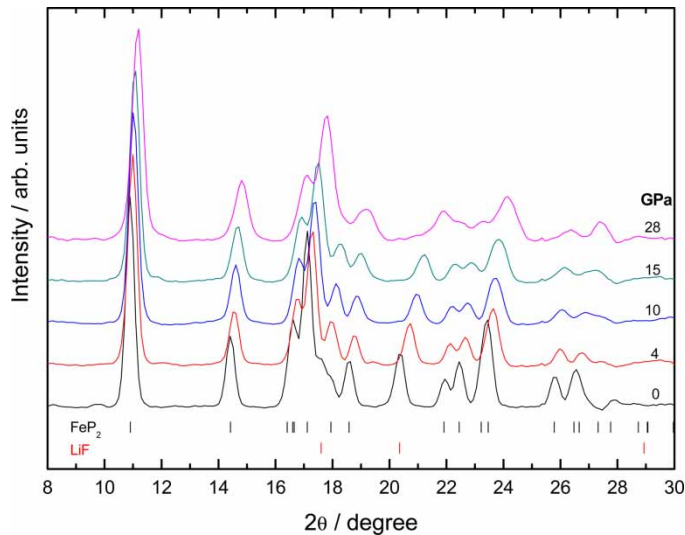


Figure 1. Some selected X-ray diffraction patterns of  $\text{FeP}_2$  at high pressure. Their backgrounds were subtracted. Vertical bars represent the positions of diffraction peaks, which are assigned to  $\text{FeP}_2$  (marcasite-type phase) and  $\text{LiF}$  ( $B1$  phase).

Table 1. Unit-cell parameters of marcasite-type  $\text{FeP}_2$  at various pressures.

$P/\text{GPa}$	$a(\text{\AA})$	$b(\text{\AA})$	$c(\text{\AA})$	$V(\text{\AA}^3)$
0.001	4.980 (3)	5.665 (3)	2.723 (1)	76.85 (5)
1	4.978 (2)	5.657 (2)	2.719 (1)	76.57 (4)
2	4.972 (4)	5.647 (3)	2.713 (1)	76.18 (5)
4	4.960 (4)	5.628 (4)	2.701 (1)	75.40 (5)
8	4.944 (3)	5.611 (3)	2.690 (1)	74.61 (4)
10	4.933 (2)	5.598 (2)	2.6763 (9)	73.91 (3)
12	4.926 (3)	5.586 (3)	2.671 (1)	73.49 (5)
15	4.918 (2)	5.573 (2)	2.6539 (9)	72.75 (3)
17	4.911 (2)	5.565 (2)	2.6433 (9)	72.24 (3)
18	4.906 (5)	5.555 (6)	2.639 (2)	71.98 (8)
20	4.901 (3)	5.544 (3)	2.627 (1)	71.38 (5)
22	4.900 (2)	5.529 (3)	2.6211 (9)	71.02 (3)
24	4.890 (2)	5.518 (2)	2.6120 (9)	70.47 (3)
26	4.881 (2)	5.509 (3)	2.6056 (9)	70.06 (3)
28	4.874 (2)	5.498 (3)	2.5991 (9)	69.66 (3)

Note: The numbers in parentheses are the estimated standard deviations in units of the last digit.

in Table 1. Both the individual unit-cell parameter and the volumes show a smooth decrease with increasing pressure. Axial compressibilities were fitted linearly by  $d = d_0 + K_d \times P$ , where  $d_0$  is the lattice constant at 0 GPa,  $K_d$  is the axial compressibility coefficient, and  $P$  is the pressure. Here we obtained  $K_a = -7.46 \times 10^{-4} \text{ GPa}^{-1}$ ,  $K_b = -1.02 \times 10^{-3} \text{ GPa}^{-1}$ , and  $K_c = -1.67 \times 10^{-3} \text{ GPa}^{-1}$  (Figure 2(a)). The  $K_c/K_a$  ratio is 2.2, and that of  $K_c/K_b$  is 1.6. Although the  $c$ -axis length is the shortest, it is the most compressible. The distinctive anisotropy of the unit-cell compressibilities is similar to that in  $\text{FeSb}_2$  in the marcasite structure [15].

The variation of the unit-cell volume with pressure was analyzed by the second-order and the third-order Birch–Murnaghan equations of state [23] using the Eosfit52 software [24]. Results of the second-order equation of state yield a unit-cell volume ( $V_0$ ) of  $76.88(6) \text{ \AA}^3$  at 0 GPa, an isothermal bulk modulus ( $B_0$ ) of  $235(3) \text{ GPa}$ , and its pressure derivative ( $B'_0$ ) of 4. Results of

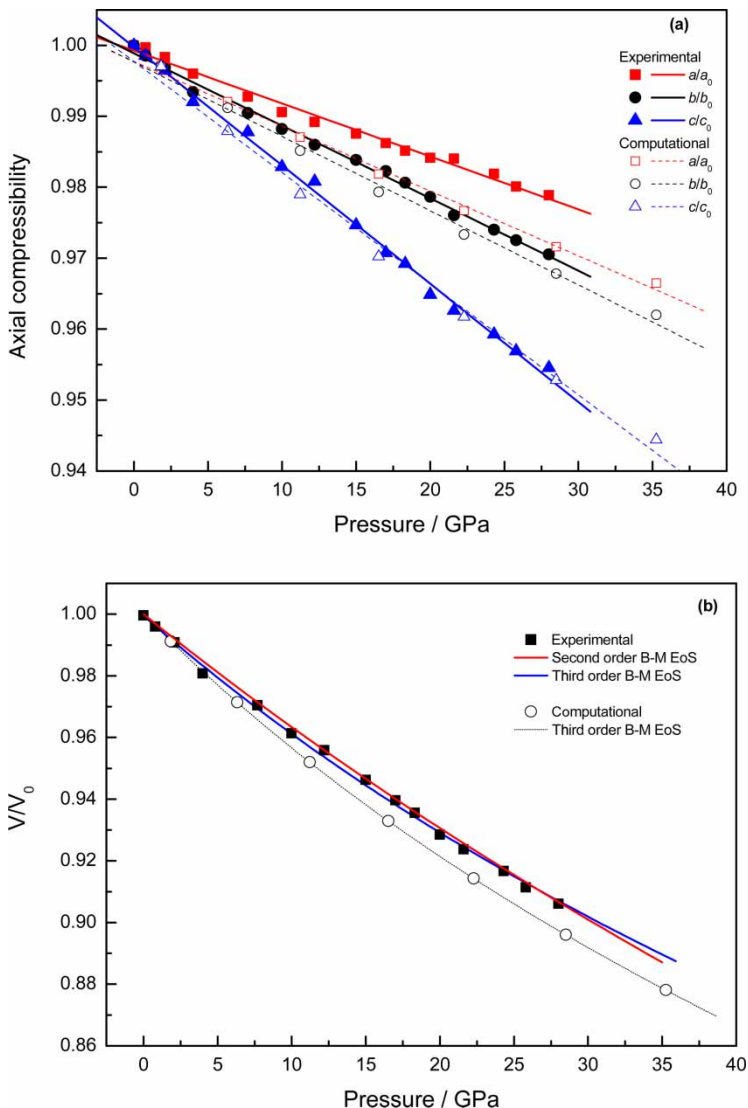


Figure 2. Compressibility of  $\text{FeP}_2$  in the marcasite structure. (a) Pressure dependence of normalized unit-cell parameters and (b) variation of  $V/V_0$  of  $\text{FeP}_2$  as a function of pressure. Solid symbols show experimental data, open symbols represent computational results.

the third-order fit are  $V_0 = 76.77(5) \text{ \AA}^3$ ,  $B_0 = 257(9) \text{ GPa}$ , and the pressure derivative of  $B_0$  at zero pressure ( $B'_0$ ) of 2.3. The second-order Birch–Murnaghan equation of state makes a more favorable comparison with the experimental data (Figure 2(b)). The bulk modulus is three times higher than that of  $\text{FeSb}_2$  (84 GPa) [15], due to the different anion size.

### 3.2. Raman spectroscopy

All Raman spectra were recorded after XRD measurements at the same pressures (except two data-points at 24 and 26 GPa). Figure 3 shows several selected spectra. At ambient condition the Raman spectrum of  $\text{FeP}_2$  exhibits four peaks located at 403.2, 433.0, 458.6, and 480.6  $\text{cm}^{-1}$ , which agrees well with the results obtained for single crystal  $\text{FeP}_2$  (403, 435, 459, and 482  $\text{cm}^{-1}$ ) [25]. Group theoretical calculation yields six Raman active phonon modes of irreducible representations, viz.  $\Gamma = 2A_g + 2B_{1g} + B_{2g} + B_{3g}$  [26]. The modes are divided into stretching modes ( $A_g + B_{1g}$ ) and librations modes ( $A_g + B_{1g} + B_{2g} + B_{3g}$ ) of the dumbbell-like P–P units. The libration modes ( $A_g + B_{2g} + B_{3g}$ ) are mixed, thus only four clear peaks are observed. The peaks (a, b, c, and d) are assigned to different Raman active modes (Table 2). Around 550  $\text{cm}^{-1}$  there is a broad feature, probably due to the effect of the second-order Raman scattering. Upon compression, all peaks shift toward high frequency, indicating a decrease of P–P bond length. Up to 28 GPa, we did not observe any splitting or merging peaks, which suggests that no phase transition occurs. Figure 4 shows the pressure dependence of phonon frequencies of Raman active modes. They were fitted linearly by  $\omega = \omega_0 + \alpha \times P$ , where  $\omega_0$  is the frequency at 0 GPa,  $\alpha$  is the linear pressure coefficient, and  $P$  is the pressure. Thus, the Grüneisen parameter ( $\gamma$ ) is obtained by  $\gamma = -\partial \ln \omega / \partial \ln V = B_0 \times \alpha / \omega_0$  [27] (Table 2).

### 3.3. Ab initio calculations

To test the structural stability of marcasite-type  $\text{FeP}_2$ , we designed several possible polymorphs, marcasite-type ( $Pnmm$ ),  $\alpha$ - $\text{PbO}_2$ -type ( $Pbcn$ ), pyrite-type ( $Pa-3$ ), and  $\text{CuAl}_2$ -type ( $I4/mcm$ ) respectively, according to the high-pressure structural behavior of the analogue compounds, e.g.

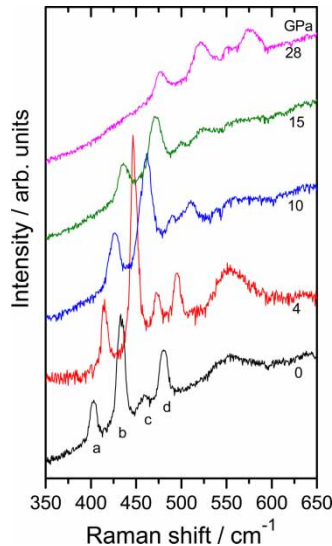


Figure 3. Selected Raman spectra of  $\text{FeP}_2$  at high pressure.

Table 2. Results of linear regressions ( $\omega$  and  $\alpha$ ) and calculated mode Grüneisen parameter  $\gamma$  using the experimental  $B_0$  (235 GPa). Fitted values (Fit.) refer to linear regression of  $\omega$  as a function of pressure (see text).

	$\omega$ (cm <sup>-1</sup> ) at 0 GPa			$\alpha$ (cm <sup>-1</sup> ) GPa <sup>-1</sup>	$\gamma$
	Ref. [23]	Observed	Fit.		
a	$A_g(\text{R})$				
	$B_{2g}(\text{R})$	403	403.2	2.49	1.45
	$B_{3g}(\text{R})$				
b	$A_g(\text{v})$	435	433.0	3.15	1.72
c	$B_{1g}(\text{R})$	459	458.6	3.15	1.61
d	$B_{1g}(\text{v})$	482	480.6	3.23	1.58

Note: R: libration mode; v: stretching vibration mode.

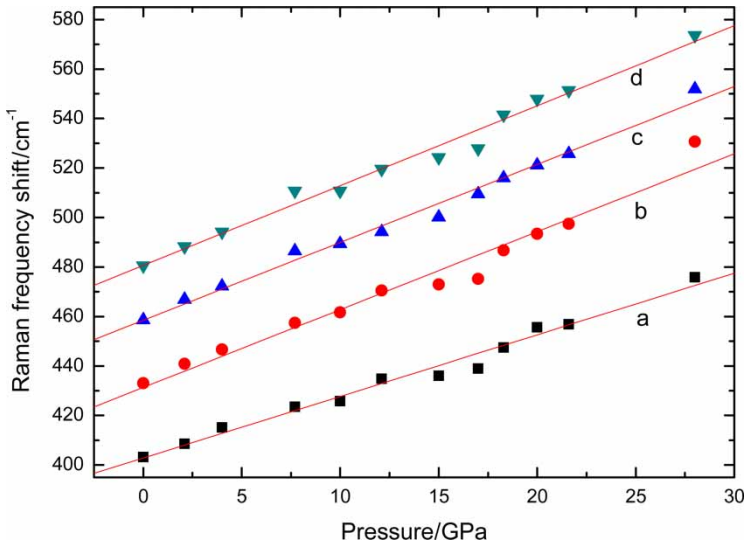


Figure 4. Variation of Raman frequency as a function of pressure. The lines are obtained by a linear fit.

GeO<sub>2</sub>, NiP<sub>2</sub>, and CrSb<sub>2</sub> [7–9,28]. All structural parameters of these phases were optimized at every computational volume. The ground-state total energy as a function of volume for the candidate phases (Figure 5) were fitted with a third-order Birch–Murnaghan equation of state. We did not find any phase transition up to 35 GPa. The equation of state parameters of marcasite-structured FeP<sub>2</sub> are  $V_0 = 68.4 \text{ \AA}^3$ ,  $B_0 = 199 \text{ GPa}$ , and  $B'_0 = 4.4$ . The  $V_0$  in LSDA-based computations is smaller than that of experimental results, following the general local density approximation (LDA) trend to underestimate the equilibrium lattice constants [29]. The theoretical axial compressibilities and  $V/V_0$  as a function of pressure are consistent with those of experiment (Figure 2).

#### 4. Discussion

In order to understand the structural evolution of marcasite-type FeP<sub>2</sub>, we further analyzed the atomic coordinates and lattice constants at various pressures. In the marcasite-type phase there are two internal structural parameters ( $x$  and  $y$  coordinates of phosphorous atom). Theoretical calculations show a decrease of  $x$  and  $y$  values at high pressure. Thus the angle from Fe to P to Fe

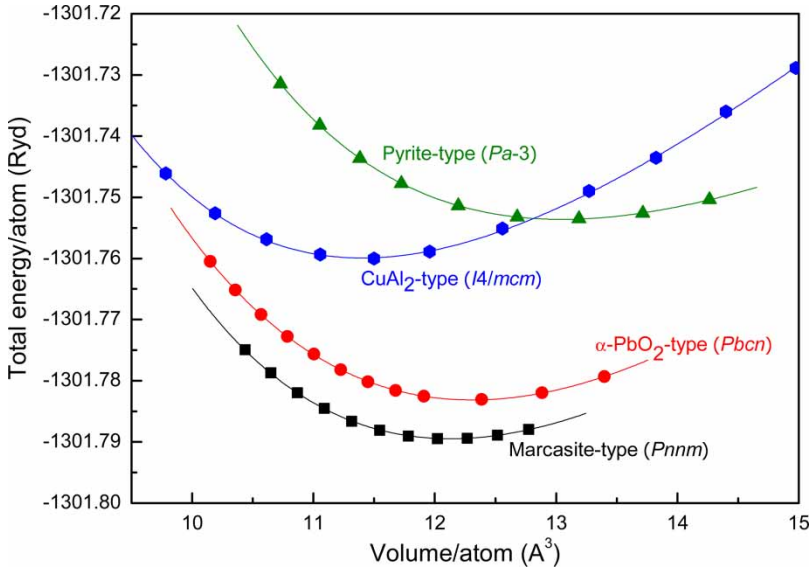


Figure 5. Calculated total energy vs. volume for candidate phases of  $\text{FeP}_2$ : marcasite,  $\alpha\text{-PbO}_2$ , pyrite, and  $\text{CuAl}_2$ .

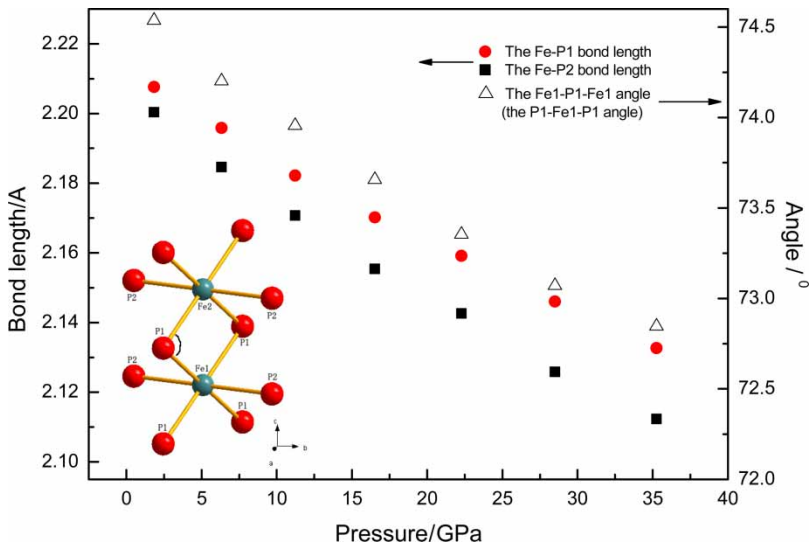


Figure 6. Bond length and bond angle vs. pressure. A fragment of marcasite-type structure showing the corresponding bond length, and bond angle is shown in the inset. Each Fe and P atoms has crystallographically equivalent positions, but they are labeled in the individual edge-sharing octahedra for discussion. The bond length corresponds to the left coordinate axes and the bond angle values are responding to the right coordinate axes.

between the edge-sharing octahedra ( $\angle\text{Fe1-P1-Fe2}$ , Figure 6) decreases from  $74.5^\circ$  at 2 GPa to  $72.8^\circ$  at 35 GPa (Figure 6). On the other hand, the Fe-P bond lengths in the  $\text{FeP}_6$  octahedra show a divergent tendency with increasing pressure (Figure 6). As a consequence, the adjacent edge-sharing octahedra become more distorted and unstable. The unit-cell compressibilities have shown that the  $c$ -axis is the most compressible. Along the  $c$ -axis, the atomic configuration is a linear chain of Fe. The electronic densities between Fe cations along the  $c$ -axis are displayed in Figure 7. Comparing them at 2 and 35 GPa, the outermost green contours of Fe cations are elongated along

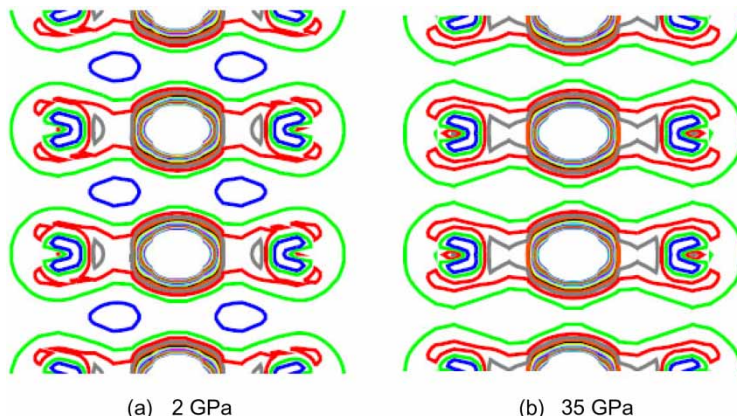


Figure 7. The valence charge density in the plane, cutting through the structural segment as shown in this figure (the P2-Fe2-P2-P2-Fe1-P2 plane). The central atom is Fe, and on both sides P atoms are located. (a) 2 GPa; (b) 35 GPa.

the  $c$ -axis with increasing pressure (color online), which indicates that the interaction between Fe atoms is enhanced. At the same time the interaction between Fe and P also increases. The electron density distribution around the Fe cation is not spherical, but elongated in the  $ab$ -plane.

In the electronic density of states (DOS) of  $\text{FeP}_2$ , the hybridization between Fe  $3d$  and P  $3p$  is observed in a wide energy range, which indicates significant covalent bond components in the  $\text{FeP}_6$  octahedra. These factors result in the edge-sharing octahedra along the  $c$ -axis becoming soft under compression. This kind of high-pressure structural behavior is different from that of anomalous marcasite with a large  $c/a$  ratio, such as  $\text{GeO}_2$  and  $\text{ZnF}_2$  [28,30]. In the anomalous marcasite-type  $\text{MX}_2$  compounds the corresponding angle ( $\angle\text{M-X-M}$ ) is greater than  $90^\circ$  and decreases toward  $90^\circ$  at high pressures, which reduces the degree of  $\text{MX}_6$  octahedra distortion, and evolves into the structures with more effective packing of  $\text{MX}_6$  octahedra.

$\text{FeP}_2$  is a semiconductor with quite a low band gap. At ambient pressure, the band gap in our calculation is 0.39 eV, very close to the 0.37 eV obtained in the single-crystal measurement [3]. At 35 GPa, the band gap is still 0.39 eV (Figure 8(a)). For a marcasite-type phase with a  $d^4$

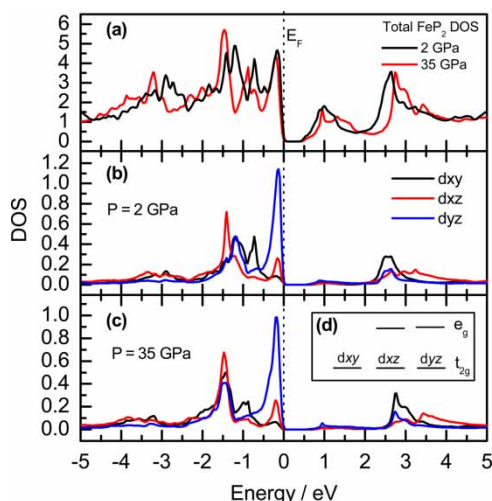


Figure 8. Total DOS of marcasite-type  $\text{FeP}_2$  at 2 and 35 GPa (a) and the partial  $t_{2g}$  DOS of Fe  $3d$  electron at 2 GPa (b) and 35 GPa (c) (color online).

configuration, Goodenough pointed out that  $t_{2g}$  orbitals are split into two lower orbitals associated with  $dxz$  and  $dyz$ , and a higher orbital associated with  $dxy$  (Figure 8(d)) [10]. The  $dxy$  states play the key role in charge conduction, because they lead to a band of itinerant electron states. In our calculations, the partial  $t_{2g}$  DOS illustrates clearly that the  $dxy$  orbital far away the Fermi level has a larger change compared with  $dxz$  and  $dyz$  with increasing pressure (Figure 8(b) and (c)), which agrees well with the description by Goodenough [10].

## 5. Conclusions

The structural stability of  $FeP_2$  at high pressure has been investigated by XRD, RS, and theoretical calculations. We did not observe any phase transition up to 28 GPa in the XRD and RS experiments. The unit-cell compressibilities of marcasite-type  $FeP_2$  represent an evident anisotropy, with the shortest axis, the  $c$ -axis, being the most compressible. The adjacent edge-sharing  $FeP_6$  octahedra become more distorted and unstable under pressure. The Raman scattering behavior of marcasite-type  $FeP_2$  at high pressure was analyzed by four peaks originating from six Raman phonon active modes. We determined their linear pressure coefficients and Grüneisen parameters. Band structure calculations within DFT show that  $FeP_2$  remains a semiconductor at pressures beyond 35 GPa.

## Acknowledgements

The authors would like to thank A. Kurnosov for his assistance in Raman and XRD experiments. X. Wu is grateful for his Alexander von Humboldt Fellowship. S. Qin acknowledges the financial support of the National Natural Science Foundation of China (Grant no. 40672024).

## References

- [1] F. Hulliger and E. Mooser, *Semiconductivity in pyrite, marcasite and arsenopyrite phases*, J. Phys. Chem. Solids 26 (1965), pp. 429–433.
- [2] F. Hulliger, *Crystal chemistry of the chalcogenides and pnictides of the transition elements*, Struct. Bonding (Berlin) 4 (1967), pp. 83–136.
- [3] G. Boda, B. Stenstrom, V. Sagredo, O. Beckman, B. Carlsson, and S. Rundqvist, *Magnetic and electric properties of  $FeP_2$  single crystals*, Phys. Scr. 4 (1971), pp. 132–134.
- [4] E. Dahl, *Refined crystal structures of  $PtP_2$  and  $FeP_2$* , Acta Chem. Scand. A 23 (1969), pp. 2677–2684.
- [5] M. Rieder, J.C. Crelling, O. Sustai, M. Drabek, Z. Weiss, and M. Klementova, *Arsenic in iron disulfides in a brown coal from the North Bohemian Basin, Czech Republic*, Int. J. Coal Geol. 71 (2007), pp. 115–121.
- [6] A. Kjekshus and T. Rakke, *Structural transformations in  $Co_tNi_{1-t}As_2$ ,  $NiAs_{2-x}S_x$ ,  $NiAs_{2-x}Se_x$ , and  $CoAs_{1-x}Se_{1+x}$* , Acta Chem. Scand. A 33 (1979), pp. 609–615.
- [7] P.C. Donohue, T.A. Bither, and H.S. Young, *High-pressure synthesis of pyrite-type nickel diphosphide and nickel diarsenide*, Inorg. Chem. 7 (1968), pp. 998–1001.
- [8] H. Takizawa, K. Uheda, and T. Endo, *A new ferromagnetic polymorph of  $CrSb_2$  synthesized under high pressure*, J. Alloys Compd. 287 (1999), pp. 145–149.
- [9] H. Takizawa, T. Yamashita, K. Uheda, and T. Endo, *High pressure crystal chemistry of transition metal diantimonides*, Phys. Stat. Sol. (b) 223 (2001), pp. 35–39.
- [10] J.B. Goodenough, *Chemical bonding in bismuth telluride*, J. Solid State Chem. 5 (1972), pp. 142–144.
- [11] G.W. Hull and F. Hulliger,  *$CuSe_2$ , a marcasite type superconductor*, Nature 220 (1968), pp. 257–258.
- [12] M. Sharon and G. Tamizhmani, *Transition metal phosphide semiconductors for their possible use in photoelectrochemical cells and solar chargeable battery (Saur Vidyut Kosh V)*, J. Mater. Sci. 21 (1986), pp. 2193–2201.
- [13] D.C.C. Silva, O. Crosnier, G. Ouvrard, J. Greedan, A. Safa-Sefat, and L.F. Nazar, *Reversible lithium uptake by  $FeP_2$* , Electrochem. Solid State Lett. 6 (2003), pp. A162–165.
- [14] C. Petrovic, J.W. Kim, S.L. Bud'ko, A.I. Goldman, P.C. Canfield, W. Choe, and G.J. Miller, *Anisotropy and large magnetoresistance in the narrow-gap semiconductor  $FeSb_2$* , Phys. Rev. B 67 (2003), pp. 155205-1–4.
- [15] C. Petrovic, Y. Lee, T. Vogt, N. Dj. Lazarov, S.L. Bud'ko, and P.C. Canfield, *Kondo insulator description of spin state transition in  $FeSb_2$* , Phys. Rev. B 72 (2005), pp. 045103-1–7.
- [16] H. Gou, L. Hou, J. Zhang, G. Sun, L. Gao, and F. Gao, *Theoretical hardness of  $PtN_2$  with pyrite structure*, Appl. Phys. Lett. 89 (2006), pp. 141910-1–3.

- [17] H.K. Mao, J. Xu, and P.M. Bell, *Calibration of ruby pressure gauge to 800 Kbar under quasi-hydrostatic conditions*, J. Geophys. Res. 91 (1986), pp. 4673–4676.
- [18] A.P. Hammersley, S.O. Svensson, M. Hanfland, A.N. Fitch, and D. Hausermann, *Two-dimensional detector software: from real detector to idealized image or two-theta scan*, High Press. Res. 14 (1996), pp. 235–248.
- [19] P. Blaha, K. Schwarz, G.K.H. Madsen, D. Kvasnicka, and J. Luitz, *WIEN2k, An Augmented Plane Wave+Local Orbitals Program for Calculating Crystal Properties*, Univ. Prof. Dr. Karlheinz Schwarz, Technische Universität Wien, Institut für Physikalische und Theoretische Chemie, Getreidemarkt 9/156 A-1060Wien/Austria, revised edition June 2002.
- [20] K. Schwarz, P. Blaha, and G.K.H. Madsen, *Electronic structure calculations of solids using the WIEN2K package for material sciences*, Comput. Phys. Commun. 147 (2002), pp. 71–76.
- [21] J.P. Perdew and Y. Wang, *Accurate and simple analytic representation of the electron-gas correlation energy*, Phys. Rev. B 45 (1992), pp. 13244–13249.
- [22] B.H. Toby, *EXPGUI, a graphical user interface for GSAS*, J. Appl. Crystallogr. 34 (2001), pp. 210–213.
- [23] F. Birch, *Elasticity and constitution of the Earth's interior*, J. Geophys. Res. 95 (1952), pp. 227–286.
- [24] R.J. Angel, *Equations of state*, in *High-pressure, high-temperature crystal chemistry*, R.M. Hazen and R.T. Downs (Eds.), Rev. Mineral. Geochem., 41 (2001), pp. 35–60.
- [25] H.D. Lutz and B. Müller, *Lattice vibration spectra. LXVIII. Single-crystal Raman spectra of marcasite-type iron chalcogenides and pnictides, FeX<sub>2</sub> (X=S, Se, Te; P, As, Sb)*, Phys. Chem. Miner. 18 (1991), pp. 265–268.
- [26] H.D. Lutz and P. Willich, *Fir-spektren und Schwingungsanalyse von FeS<sub>2</sub>-markasit*, Z. Naturforsch 30a (1975), pp. 1458–1461.
- [27] M. Blackman, *On the thermal expansion of solids*, Proc. Phys. Soc. London Sect. B 70 (1957), pp. 827–832.
- [28] V.P. Prakapenka, G. Shen, L.S. Dubrovinsky, M.L. Rivers, and S.R. Sutton, *High pressure induced phase transformation of SiO<sub>2</sub> and GeO<sub>2</sub>: difference and similarity*, J. Phys. Chem. Solids 65 (2004), pp. 1537–1545.
- [29] X. Wu, S. Qin, and Z.Y. Wu, *First-principles study of structural stabilities, and electronic and optical properties of CaF<sub>2</sub> under high pressure*, Phys. Rev. B 73 (2006), pp. 134103-1–8.
- [30] X. Wu and Z.Y. Wu, *Theoretical calculations of the high-pressure phases of ZnF<sub>2</sub> and CdF<sub>2</sub>*, Eur. Phys. J. B 50 (2006), pp. 521–526.